Capture-gated fast neutron spectroscopy with a composite scintillator

Hong-Zhao Zhou,[1] Tao Sun,[1] Hai-Xia Liu,[1] Yi-Na Liu,[2] Ye Chen,[1]
Chong-Wei Li,[1] Xian Guan,[1] Dong-Xi Wang,[1] and Wu-Yun Xiao[1,*]

[1]*State Key Laboratory of NBC Protection for Civilian, Beijing 102205, China*
[2]*China Institute of Atomic Energy, Beijing 102413, China*

Recoil fast neutron spectroscopy with organic scintillators is troubled by the difficulty of spectrum unfolding, which is caused by the flat response to mono-energetic neutrons. Capture-gated (CG) fast neutron spectroscopy with composite scintillators is promising to address this problem as capture-gated events raise a characteristic peak in the response. Nevertheless, the realization of CG fast neutron spectroscopy was prevented by the poor discrimination performance of present composite scintillators and short of influence elimination of chance coincidence events. In this paper, CG fast neutron spectroscopy was fully realized for the first time based on the composite scintillator proposed in our previous work. Results show that this spectroscopy has a suitable energy range from about 0.4 MeV to 20 MeV. For the ^{241}Am–Be source, iterations of recoil and CG spectrum unfolding using flat default spectrum are 10 000 and 380, respectively. With the simulated spectrum as reference, R^2 of recoil and CG unfolded spectra are respectively 0.939 and 0.975 above 1 MeV. These results reflect that CG fast neutron spectroscopy significantly alleviates the difficulty of spectrum unfolding and exhibits better energy resolution and precision. This work can be applied in neutron metrology laboratories and other nuclear facilities.

Keywords: Fast neutron spectroscopy, Composite scintillator, Capture-gated event, Response matrix, Spectrum unfolding

I. INTRODUCTION

Neutron monitoring is necessary in nuclear science and industry since nuclear fission, fusion and spallation release plenty of neutrons. Energy spectrum of fluence reveals the energy distribution of neutrons. It can be used to calculate quantities including fluence rate, average energy and radiation dose. Therefore, neutron spectroscopy is a significant part of neutron monitoring. Nuclear fission, fusion and spallation mainly release fast neutrons, whose fluence-dose conversion coefficients are much higher than those of slow neutrons [1]. Consequently, fast neutrons usually dominate neutron dose, while fast neutron spectroscopy is significant to monitor the operation of neutron facilities, such as nuclear power plant [2], fusion tokamak [3], spallation neutron source [4], space station [5] and neutron metrology laboratory [6].

Despite time of flight, fast neutron spectrum is usually measured with spectrometers or detectors via neutron moderation, reaction and scattering [7]. The first category mainly refers to Bonner sphere spectrometer (BSS) [8], which is characterized by the broad applicable energy range from 0.025 eV to even 10 GeV [9]. However, the multiple moderation spheres make BSS bulky, while the energy resolution is poor due to few-channel unfolding. Similar to BSS, multi-foil activation technique [10] and superheated drop detectors [11] also require few-channel unfolding. Multi-foil activation technique is usually used to monitor neutrons in nuclear reactors [12], which can also be theoretically calculated [13]. Detectors of the second category include ^{3}He proportional counter [14], CLYC scintillator [15] and diamond detector [16]. These detectors have better energy resolutions than BSS because their response spectra to mono-energetic neutrons contain characteristic peaks. Nevertheless, the small cross-section for fast neutrons hinders their usage. Detectors of the last category usually relies on hydrogen to scatter fast neutrons and release recoil protons, such as hydrogen-filled proportional counters [17], proton-recoil telescopes [18], and organic scintillators [19]. Compared with other neutron detectors, organic scintillators are characterized by high sensitivity to fast neutrons, excellent n/γ discrimination performance, short decay time and low cost. These advantages contribute to the wide usage of organic scintillators in recoil fast neutron spectroscopy [20–22].

As the quenching effect depends on energy loss density [23], organic scintillators have nonlinear light output for protons. Besides, the isotropic scattering from hydrogen below 10 MeV [7] results in a flat response to mono-energetic neutrons, making spectrum unfolding difficult. The first issue can be resolved through the calibration of light output in a neutron field with a broad energy distribution using time of flight [24]. To address the second issue, ^{10}B (or ^{6}Li) were doped into liquid and plastic scintillators [25, 26]. In these doped scintillators, it is possible that the incident fast neutron first creates a recoil pulse through scattering from hydrogen, and then gives rise to a capture pulse after the thermalized neutron is captured by ^{10}B (or ^{6}Li). The correlated recoil and capture pulses constitute a capture-gated event (CGE) [27], which can be recognized through time coincidence. As the kinetic energies of captured neutrons are usually negligible, CGEs exhibit a unique signature that can be used to single out just those neutrons that transfer all their energy to recoil protons. Therefore, a characteristic peak emerges in the capture-gated (CG) spectrum formed by the recoil pulses of CGEs to mono-energetic neutrons. CG fast neutron spectroscopy takes advantage of this feature and is able to alleviate the difficulty of spectrum unfolding.

Doping ^{10}B (or ^{6}Li) will aggravate the quenching effect [28] and degrade light output as well as n/γ discrimi-

* Corresponding author, xiaowuyun@sklnbcpc.cn

nation performance [25], making it difficult to identify capture pulses and coincidence events. To avoid this problem, segmented spectrometers [29, 30] and composite scintillators [31, 32] were proposed, which combine organic scintillators with ^{3}He proportional tubes and ^{10}B (or ^{6}Li) loaded inorganic scintillators, respectively. As the organic and inorganic scintillators use the same photomultiplier tube (PMT) and electronic circuit, composite scintillators are usually more compact than segmented spectrometers. Capture pulses generated in inorganic scintillators have distinct shape from recoil pulses generated in organic scintillators. Therefore, capture pulses and coincidence events can be easily recognized. Based on composite scintillators, coincidence events consisting of CGEs and chance coincidence events (CCEs) have been identified [33], while the characteristic peak in coincidence spectrum to mono-energetic neutrons has been verified [33, 34]. However, present composite scintillators are mainly based on plastic scintillators, making it difficult to distinguish neutrons from γ-rays. Besides, the influence of CCEs on coincidence spectrum should be eliminated. These issues inhibit the realization of CG fast neutron spectroscopy.

In our previous work [35], a stilbene-lithium glass composite scintillator was proposed. This detector exhibits much better triple discrimination performance than composite scintillators based on plastic scintillators [32, 33, 36–38]. Coincidence events were recognized from the pulses generated by this detector. CG spectrum was calculated through subtraction of chance coincidence (CC) spectrum formed by CCEs from coincidence spectrum [39]. Subtraction of CC spectrum is necessary since CCEs usually dominate coincidence events. Triple discrimination is required to identify CCEs caused by γ-ray and capture pulses. In this paper, CG fast neutron spectroscopy will be fully realized to obtain the energy spectrum of fast neutron fluence, based on the proposed detector and the acquisition method of CG spectrum. Recoil fast neutron spectroscopy which utilizes recoil pulses without coincidence will also be realized for comparison.

II. FAST NEUTRON SPECTROSCOPY PRINCIPLE

The proposed composite scintillator is based on a $\phi 4\,\mathrm{cm}\times 4\,\mathrm{cm}$ stilbene crystal. Each end surface of the stilbene crystal is covered by a piece of $\phi 4\,\mathrm{cm}\times 1\,\mathrm{mm}$ lithium glass. One piece of lithium glass is coupled with a $\phi 5.08\,\mathrm{cm}$ ETL 9266 PMT. As shown in Fig. 1, recoil, γ-ray and capture pulses are generated and digitalized with neutrons and γ-rays vertically entering the end surface of the detector. Recoil and γ-ray pulses are stimulated in stilbene while capture pulses are generated in lithium glass. Due to the small thickness, γ-ray pulses generated in lithium glass are below the threshold and will not be recorded.

Measured spectrum can be expressed as:

$$N = \boldsymbol{R}\Phi, \tag{1}$$

where $\boldsymbol{R}$ is the convolution of response matrix and Φ is the energy spectrum of fluence. $\boldsymbol{R}$ is constituted by a series of response spectra to mono-energetic neutrons with different energies. The goal of fast neutron spectroscopy is to obtain the energy spectrum of fluence for fast neutrons through spectrum unfolding, which is the process of deconvolution conducted with measured spectrum and response matrix. For the composite scintillator, there are two kinds of fast neutron spectroscopy. Recoil fast neutron spectroscopy is the conventional method of common organic scintillators. It requires recoil spectrum unfolding conducted with measured recoil spectrum and recoil response matrix. As a specific method of composite scintillator, CG fast neutron spectroscopy requires CG spectrum unfolding conducted with measured CG spectrum and CG response matrix.

Given the digitalized pulses, measured recoil spectrum is formed by recoil pulses which are identified through triple discrimination. Coincidence events are recognized through time coincidence. Coincidence recoil events consisting of CGEs and recoil CCEs can survive triple discrimination. As the two pulses of each CCE are uncorrelated, recoil CC spectrum has the same distribution as the recoil spectrum measured without time coincidence. Its strength can be calculated with the counts of capture CCEs and capture events collected without time coincidence. Measured CG spectrum is obtained through the subtraction of recoil CC spectrum from coincidence recoil spectrum which is formed by coincidence recoil events. The detector's response matrix is usually established through Monte Carlo (MC) simulation.

III. SPECTRUM MEASUREMENT

The detector's recoil and CG spectra to mono-energetic neutrons and neutrons with broad energy distributions were respectively measured. Measured spectra to mono-energetic neutrons were used to verify MC simulation and check the feasibility of recoil and CG fast neutron spectroscopy. Measured spectra to neutrons with broad energy distributions were used for recoil and CG spectrum unfolding. Pulses were collected and processed offline to implement triple discrimination and spectrum recording.

A. Pulse collection

The detector worked at $-810\,\mathrm{V}$ bias voltage and was powered by an Iseg SHR4060 desktop power supply. Pulses were collected with a CAEN DT5730 digitizer under the control of the CoMPASS software. The digitizer has a resolution of 14 bits and a sampling rate of 500 MS/s. Each pulse contained 200 samples. Trigger threshold was set to 30 LSB, which was equivalent to about 50 keVee. Energy calibration was performed with a ^{152}Eu γ source through Compton coincidence measurement [40] in our previous work [35]. Long-gate for the calculation of pulse amplitude was set to $300\,\mathrm{ns}$.

In order to obtain measured spectra to mono-energetic neutrons, pulse collection measurements were conducted in the reference mono-energetic neutron radiation fields at China institute of atomic energy. Neutron fields with energies of

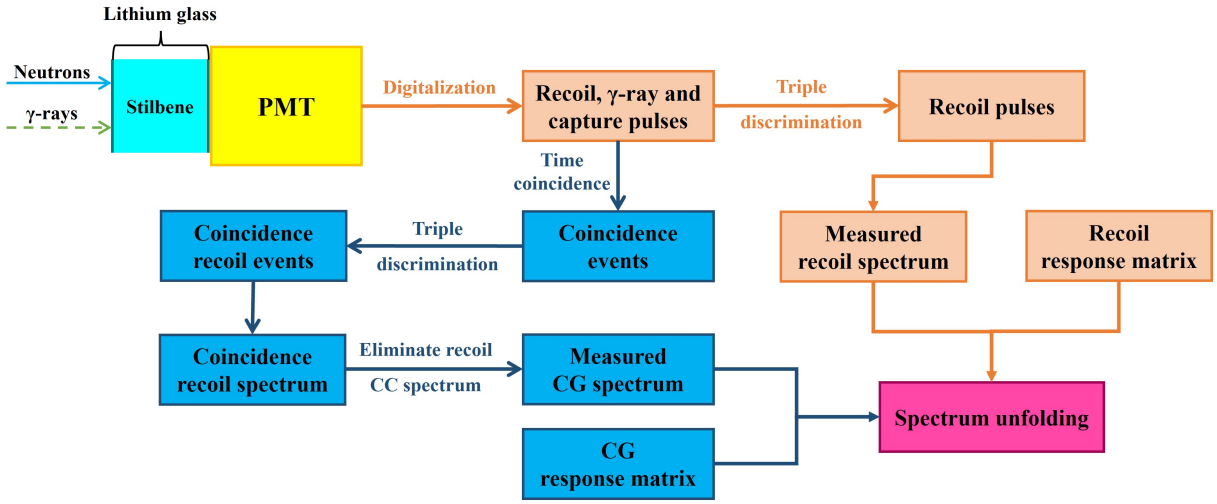

Fig. 1. Schedule of fast neutron spectroscopy with the composite scintillator

1.2 MeV, 2.5 MeV, 5 MeV and 14.84 MeV were generated by a tandem accelerator. The detector was placed 123.5 cm away from the target at the same level. Pulses caused by room-scattered neutrons were recorded after a shadow cone was placed 10 cm away from the target along the detector-target axis. The shadow cone was made of 20 cm iron and 30 cm boron-loaded polyethene.

For spectrum measurements to neutrons with broad energy distributions, neutron fields were separately generated by an ^{241}Am–Be and ^{252}Cf in the State Key Laboratory of NBC Protection for Civilian. The current neutron emission rates of the two sources were respectively 4.19×10^7 s^{-1} and 9.86×10^8 s^{-1} after decay correction. A lead brick with a thick of 5.2 cm was placed nearby the source tube in order to absorb γ-rays and increase the probability of CGEs. Source-detector distance was 1.2 m for the ^{241}Am–Be source. For the ^{252}Cf source, this distance was lengthened to 2 m due to the higher neutron emission rate. Shadow cones consisting of 20 cm iron and 30 cm boron-loaded polyethene were used to collect pulses produced by room-scattered neutrons.

B. Spectrum recording

Each pulse was discriminated through linear separation method [41]. Pulse height spectra formed by recoil pulses without time coincidence were recorded. They were then converted into measured recoil spectra using energy calibration. The influence of room-scattering was eliminated through the subtraction of the spectrum formed by room-scattered neutrons from the measured recoil spectrum.

To obtain measured CG spectra, the timing gate of time coincidence was set to 20 μs according to our previous work [39]. For each capture pulse, its previous pulse was checked. If the time difference of the two adjacent pulses was less than the timing gate, these two pulses were recognized as a coincidence event, which could be a CGE or a CCE. The previous pulse of a CCE is randomly caused by recoil protons, γ-ray or neutron capture. Therefore, coincidence events can be divided into γ-ray CCEs, capture CCEs, recoil CCEs and CGEs. γ-ray CCEs and capture CCEs were easily identified through triple discrimination. However, recoil CCEs and CGEs were mixed together since their previous pulses were intrinsically identical. Consequently, CGEs could not be recognized one by one. As recoil CC spectrum and CG spectrum have different distributions, the influence of recoil CCEs was eliminated through spectrum subtraction. Recoil CC spectrum was calculated as follow:

$$S_{\mathrm{CCE,rec}} = S_{\mathrm{rec}} C_{\mathrm{CCE,cap}} / C_{\mathrm{cap}}, \tag{2}$$

where S_{rec} is the recoil spectrum obtained without time coincidence, while $C_{\mathrm{CCE,cap}}$ and C_{cap} are respectively the counts of capture CCEs and capture events without time coincidence. The requirement of coincidence and subtraction of recoil CC spectrum greatly reduces CGE efficiency.

IV. RESPONSE MATRIX ESTABLISHMENT

Recoil and CG response matrices were simulated using the Geant4 [42] MC toolkit. The amplitudes of measured pulses are affected by light output fluctuation, light transmission, light-electron conversion and electronic noise. These factors can smear the spectrum and their influence is represented by energy resolution. To keep simulated spectra consistent with measured ones, energy resolution of the detector was calibrated. Besides, light output function was characterized in order to calculate the light output according to the energies of secondary charged particles. Light output was expressed in MeVee, a unit of electron equivalent energy. MC simulations were verified through comparison of measured recoil and CG spectra to mono-energetic neutrons with simulated ones.

A. Energy resolution

For the total light output L, energy resolution can be calculated as:

$$\frac{\Delta L}{L} = \sqrt{a_1^2 + \frac{a_2^2}{L} + \frac{a_3^2}{L^2}}, \tag{3}$$

where ΔL is the full width at the half maximum (FWHM) of L, while a_1, a_2 and a_3 are parameters to be determined.

Four γ sources including ^{137}Cs, ^{60}Co, ^{152}Eu and ^{22}Na were used to calibrate the detector's energy resolution, since the response of organic scintillators to electrons is linear for particle energy above about 125 keV [7]. For other detectors such as NaI(Tl), energy resolution is usually calibrated through full energy peaks. However, the composite scintillator has low atomic number and full energy peaks cannot be recognized in its γ spectra. Compton coincidence measurement was implemented to make characteristic peaks emerge at Compton edges. The energy of Compton edge was calculated as:

$$E_c = \frac{2E_\gamma^2}{m_e c^2 + 2E_\gamma}, \tag{4}$$

where E_γ is the energy of incident γ-rays and $m_e c^2$ is the rest energy of electron. A $\phi 5.08\,\mathrm{cm} \times 5.08\,\mathrm{cm}$ BaF_2 detector was placed 32 cm against the composite scintillator to detect γ-rays scattered from stilbene. Measurements were carried out with the four γ sources successively fixed 2 cm against the composite scintillator. These two distances were optimized to balance the count rate and the solid angle of the composite scintillator.

Similar to the measurement of CGEs, Compton coincidence measurement also belongs to time coincidence. Therefore, coincidence events generated by the composite scintillator contain true coincidence events (TCEs) and CCEs. For γ-rays with a certain energy, TCEs approximately share the same amplitude and constitute a characteristic peak at Compton edge in the true coincidence (TC) spectrum. CCEs follow the same distribution as the spectrum obtained without coincidence. Consequently, the continuum in coincidence spectrum is caused by CCEs. Using Eq. (2), CC spectrum was calculated with the spectrum measured without coincidence and the counts over the continuum region with and without coincidence. Then CC spectrum was subtracted from coincidence spectrum to obtain TC spectrum.

^{22}Na has a probability of 90.20% to undergo β^+ decay, and positron annihilation will release two opposite 511 keV γ-rays. If one 511 keV γ-ray enters the composite scintillator, the other one will probably enter the BaF_2 detector. It will trigger an annihilation coincidence (AC) event. AC spectrum has the same distribution with the spectrum caused by 511 keV γ-rays without coincidence. After the subtraction of CC spectrum for ^{22}Na, AC spectrum should also be removed.

The upper row of Fig. 2 shows that after the subtraction of CC and AC spectra from Compton coincidence spectra (labeled as "Total"), TC spectra exhibit clear characteristic peaks at Compton edges for all the four γ sources. The proportion of CC spectrum depends on the number and emission probabilities of γ-rays. ^{137}Cs requires at least two decays to form a CCE since it releases a 661.66 keV photon in each decay. Therefore, the proportion of CC spectrum for ^{137}Cs is significantly lower than those for the other three sources.

Due to the non-zero dimensions of the two detectors, Compton scattering with a scattering angle slightly below 180° can also trigger a coincidence event. Therefore, the deposited energy spectrum of TCEs (S_{DES}) is actually a peak rather than a line. True coincidence peaks in the upper spectra of Fig. 2 are affected by S_{DES} and energy resolution. S_{DES} was simulated with Geant4 in order to obtain its width. FWHM corresponding to energy resolution was computed:

$$\Delta L = \sqrt{\mathrm{FWHM}_{\mathrm{TCP}}^2 - \mathrm{FWHM}_{\mathrm{DES}}^2}, \tag{5}$$

where $\mathrm{FWHM}_{\mathrm{DES}}$ is the FWHM of S_{DES}, and $\mathrm{FWHM}_{\mathrm{TCP}}$ is the FWHM of the true coincidence peak. Aiming to determining a_1, a_2 and a_3, Eq. (3) was used to fit the FWHMs which were calculated according to the true coincidence peaks. Then S_{DES} without coincidence was broadened by energy resolution and simulated spectrum was obtained. The lower row of Fig. 2 shows that all the simulated spectra agree well with the measured ones. It indicates that the parameters of energy resolution are correct.

B. Light output function for protons

As scintillation lights of organic scintillators are mainly stimulated by recoil protons, light output function for protons $L_p(E)$ is critical to obtain correct simulated spectra, where E represents the energy of protons. As the $L_p(E)$ presented in the literature [43] resulted in discrepancy between simulated and measured spectra below 5 MeV, a new $L_p(E)$ was established with measured recoil spectra to mono-energetic neutrons.

Typical of many organic scintillators, $L_p(E)$ can be represented as proportional to $E^{3/2}$ for energies below about 5 MeV, and becomes approximately linear for higher energies [7]. For measured recoil spectrum to neutrons with energy of E_n, $L_p(E_n)$ and $M(E_n)$ can be determined through the first derivative of the spectrum [44], where $M(E_n)$ refers to the light output corresponds to the local maximum in the multi-scattering region. Simulations show that incident neutrons tend to transfer all their energy to recoil protons in multi-scattering. Therefore, $M(E_n)$ represents the minimum total light output of the recoil protons whose total kinetic energy is E_n. As $L_p(E)$ is a convex function, $M(E_n)$ can be calculated:

$$M(E_n) = 2L_p(E_n/2) \tag{6}$$

Given $L_p(E_n)$ and $M(E_n)$, the new $L_p(E)$ was established as follow

$$L_p(E) = \begin{cases} 0.18075E^{3/2}, & E \le 5\ \mathrm{MeV} \\ -1.16861 + 0.63789E, & E > 5\ \mathrm{MeV} \end{cases} \tag{7}$$

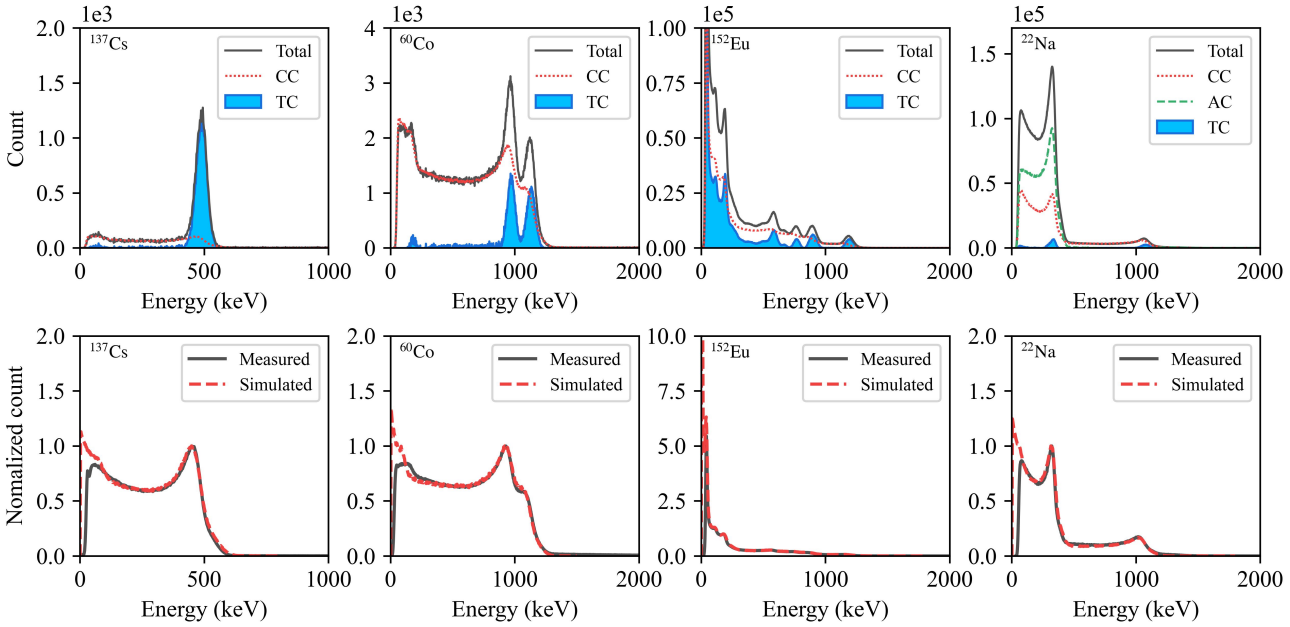

Fig. 2. Decomposition of Compton coincidence spectra (upper row) and comparison of measured and simulated γ spectra without coincidence (lower row)

C. Monte Carlo simulation

The composite scintillation detector was modeled with the Geant4-10.7.2 toolkit. Each of the two end surfaces of the $\phi 4\,\mathrm{cm}\times 4\,\mathrm{cm}$ stilbene crystal was connected by a piece of $\phi 4\,\mathrm{cm}\times 1\,\mathrm{mm}$ lithium glass. The front and surrounding surfaces of the composite scintillator were covered by $0.4\,\mathrm{mm}$ aluminum. PMT was neglected since it had little influence on neutron transportation in stilbene and lithium glass. Mono-energetic neutrons perpendicularly entered the detector. Their positions were randomly sampled from a $\phi 4.08\,\mathrm{cm}$ disc, which was $5\,\mathrm{cm}$ away from the end surface. The recommended PhysicsList `FTFP_BERT_HP` was used for neutron transportation below $20\,\mathrm{MeV}$. CENDL-3.1 [45] library was used to provide neutron cross-sections since the built-in G4NDL library was short of cross-section for the $^{12}\mathrm{C}(\mathrm{n},\mathrm{n}')\,3\,\alpha$ reaction [24]. For each run, the number of primary neutrons was $\lceil E_\mathrm{n}\rceil \times 10^8$ in order to keep the statistical error of total count below 3%, where $\lceil E_\mathrm{n}\rceil$ is the ceil integer with E_n in the unit of MeV.

In the `SteppingAction` class, the kinetic energies of each proton track before and after a step created in stilbene were read as E_pre and E_post. Using Eq. (7), the light output generated along this step L_step was represented as $L_\mathrm{p}(E_\mathrm{pre}) - L_\mathrm{p}(E_\mathrm{post})$. The light outputs for other charged particles were calculated in a similar way and their light output functions were identical to our previous work [35]. The initial time t_1 when light output was generated in stilbene was labeled as the first gate of CGE. In the `StackingAction` class, the α track created in the two pieces of lithium glass represented the $^6\mathrm{Li}(\mathrm{n},\alpha)\,^3\mathrm{H}$ reaction. The corresponding time t_2 was labeled as the second gate of CGE. L_step, t_1 and t_2 were written into the `EventAction` class after their values were determined. At the end of each event, standard deviation σ was computed using Eq. (3) with the total light output L_total. Light output broadened by energy resolution L_reso was sampled from a Gaussian distribution with a mean value of L_total and standard deviation of σ. L_reso was written into the histogram H_1 to record simulated recoil spectrum. If t_1 and t_2 were both set, L_reso was also written into the histogram H_2 to record simulated CG spectrum. At the end of each run, H_1 and H_2 were saved into files.

D. Comparison of measured and simulated spectra

The upper row of Fig. 3 shows measured and simulated recoil spectra to neutrons with four energies. Each spectrum was normalized by the count at $M(E_\mathrm{n})$. The good agreement between simulated and measured spectra validates MC simulations and the parameters of energy resolution. All the recoil spectra exhibit a continuum due to the energy variation of recoil protons under different scattering angle. As $L_\mathrm{p}(E)$ is basically proportional to $E^{3/2}$ below $5\,\mathrm{MeV}$, recoil spectrum is approximately proportional to $L^{-1/3}$. Thus, counts increase as L decreases.

There are two edges in each recoil spectrum. The right edge represents $L_\mathrm{p}(E_\mathrm{n})$ and is smeared by energy resolution. The left edge represents $M(E_\mathrm{n})$ and is caused by multi-scattering from hydrogen. If recoil protons have a fixed total kinetic energy E_k, the total light output of multi-scattering L_mul is affected by the distribution of kinetic energy. L_mul reaches its maximum L_max when E_k is transferred to one proton. It means that multi-scattering becomes single-scattering. L_mul reaches its minimum L_min when all the recoil protons have equal kinetic energy. Therefore, L_mul is a distribution

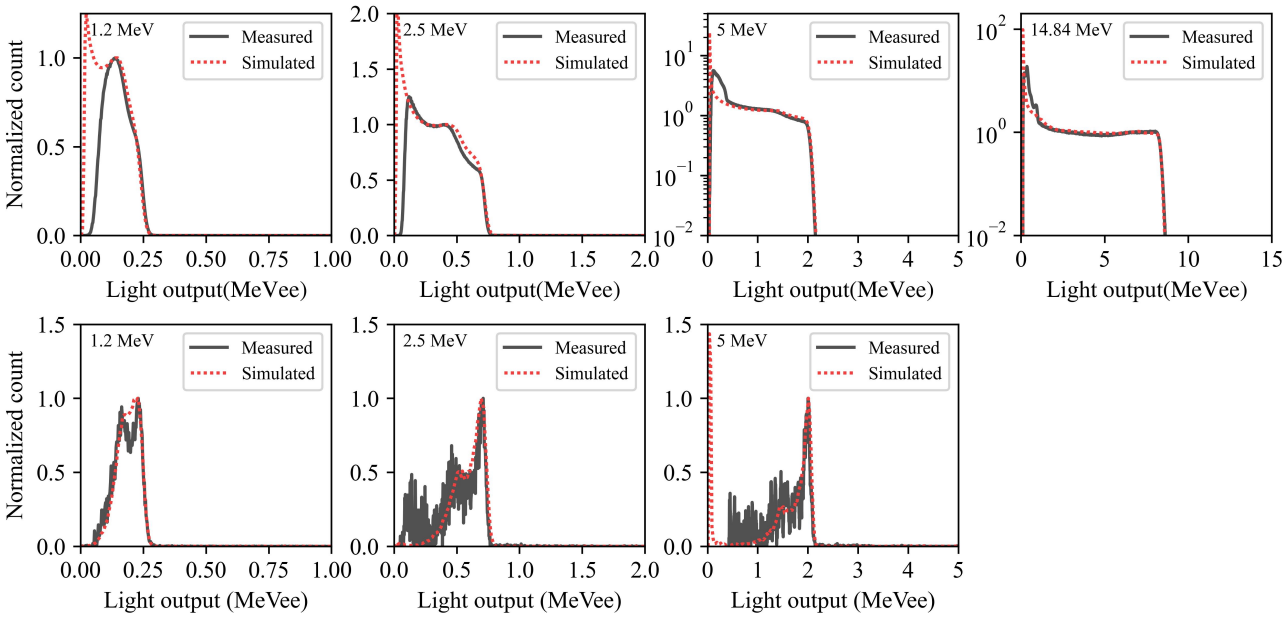

Fig. 3. Comparison of measured and simulated spectra to mono-energetic neutrons. The upper row exhibits recoil spectra and the lower row exhibits CG spectra.

ranging from $L_{\min}$ to $L_{\max}$. The recoil spectrum caused by multi-scattering is the convolution of the energy distribution and L_{mul}. Above $M(E_{\mathrm{n}})$, the energy range that contributes to the recoil spectrum gradually shrinks. Consequently, recoil spectrum encounters a evident decline after $M(E_{\mathrm{n}})$, and a local maximum appears at $M(E_{\mathrm{n}})$.

The lower row of Fig. 3 shows measured and simulated CG spectra to neutrons with energies of first three energies. Spectra to $14.84\,\mathrm{MeV}$ neutrons were discarded since the measured CG spectrum was troubled by low counts and failed to show explicit distribution. Each spectrum was normalized by the count at $L_{\mathrm{p}}(E_{\mathrm{n}})$.

Compared with the recoil spectrum, the most significant distinction of the CG spectrum is that a characteristic peak appears at $L_{\mathrm{p}}(E_{\mathrm{n}})$. It verifies the selection effect of CGEs on the amplitude of recoil pulses. The good agreement between simulated and measured spectra reflects that CG spectra were correctly simulated. The local maximum at $M(E_{\mathrm{n}})$ caused by multi-scattering in CG spectrum is more apparent than that in recoil spectrum. As the number of CCEs is remarkably higher than that of CGEs, subtraction of CC spectrum results in fluctuation at the left side of the characteristic peak. This phenomenon becomes more obvious for the latter two energies since the probability of CGEs goes down as neutron energy increases. Besides, some γ-rays could be mislabeled as neutrons because n/γ discrimination becomes ambiguous when L is small.

E. Response matrices

Recoil and CG spectra were simulated with Geant4. Light output of these spectra ranges from 50 keVee to 11.95 MeVee, with an interval of 50 keVee. The lower limit of light output was set to discard noise and ambiguous pulses. Energy of incident neutrons grows from $400\,\mathrm{keV}$ to $20\,\mathrm{MeV}$, with an interval of $100\,\mathrm{keV}$. The lower limit of neutron energy approximately corresponds to the lower limit of light output. All the spectra were normalized by incident neutron fluence. Response matrix was constructed with the simulated spectra ranked in ascending order of neutron energy. Each column of the matrix represents a spectrum. Fig. 4 illustrates the two response matrices in which neutron energy covers $1\,\mathrm{MeV}$ to $20\,\mathrm{MeV}$, with an interval of $1\,\mathrm{MeV}$.

In recoil response matrix, each recoil spectrum can be separated into three stages as light output increases. At the first stage, recoil spectrum is mainly formed by recoil carbons and low-energetic protons. This stage is characterized by high counts and fast descent. At the second stage, recoil spectrum is dominated by recoil protons possessing a various total energy transferred by incident neutrons. Recoil spectrum is flat at this stage due to the isotropic cross-section for neutron elastic scattering from hydrogen. As incident neutron energy increases, the maximum light output is elevated and the count in each bin falls. The last stage begins from $L_{\mathrm{p}}(E_{\mathrm{n}})$. At this stage, the incident neutron transfers almost all its energy to recoil protons. Then the thermalized neutron is captured by a hydrogen nucleus and a deuterium nucleus is created. A $2.22\,\mathrm{MeV}$ γ-ray is then released in the deactivation of the deuterium nucleus. Scintillation lights stimulated by recoil protons and the $2.22\,\mathrm{MeV}$ γ-ray generate a mixed pulse together. Recoil protons basically stimulate a fixed total number of lights. However, the scintillation lights stimulated by the $2.22\,\mathrm{MeV}$ γ-ray depend on the Compton scattering angle. It results in the amplitude variation of mixed pulses. The probability of mixed pulse is very low since counts at the last stage

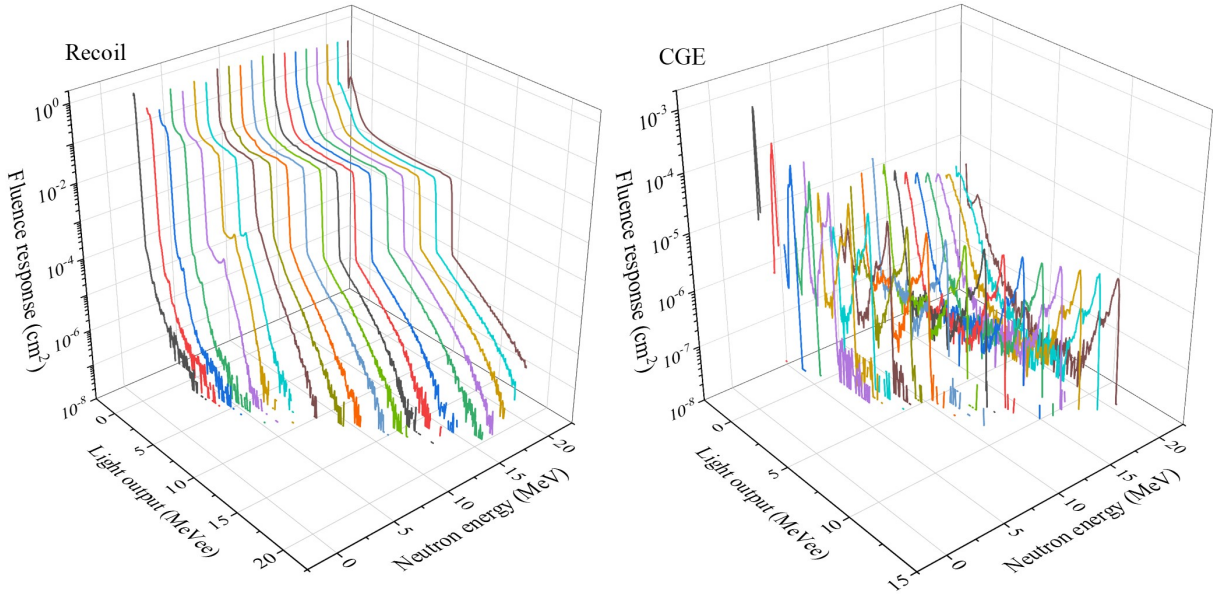

Fig. 4. Recoil and CG response matrices

are much lower than those at the second stage. Therefore, the last stage has little influence on spectrum unfolding.

In CG response matrix, each CG spectrum contains a characteristic peak at $L_{\mathrm{p}}(E_{\mathrm{n}})$. A ridge line is converged by the characteristic peaks of different CG spectra. This ridge line is a clear distinction of the two matrices and helpful to alleviate the difficulty of spectrum unfolding. The probability of CGEs and the characteristic peak fall as incident neutron energy increases. CGEs discard the event in which the incident neutron escapes without having lost all its energy. Therefore, counts at the first stage are relatively low, while counts at the second stage are concentrated in the peak area. The $2.22\,\mathrm{MeV}$ γ-ray will not happen since CGEs require that the thermalized neutrons are captured by ^{6}Li. Thus, counts at the last stage are basically zero. Due to the low probability of CGEs, counts in CG response matrix are smaller than those in recoil response matrix by about three orders of magnitude.

V. SPECTRUM UNFOLDING

Given measured spectrum and response matrix, spectrum unfolding can be realized. Recoil and CG spectrum unfolding was respectively performed with measured recoil and CG spectra to mono-energetic neutrons, aiming to verify the feasibility of spectrum unfolding. As neutrons at the practical workplace usually have various energies, recoil and CG spectrum unfolding was then respectively performed with measured recoil and CG spectra to neutrons with a broad energy distribution.

A. Implementation of spectrum unfolding

In this paper, spectrum unfolding was performed with the MAXED [46] code from the UMG3.1 toolkit, which was developed by the Physikalisch-Technische Bundesanstalt. This code applies the maximum entropy principle. It takes a default spectrum as the initial estimate and enters an iteration loop in order to optimize the solution based on measured spectrum and response matrix. The code will be terminated when the chi-square or iteration number reach the preset limits.

The iteration limit was set to $10\,000$, which was large enough for convergence. Light output for measured spectrum and columns of the response matrix ranged from 0.05 MeVee to 11.95 MeVee. Neutron energy for default spectrum and rows of the response matrix ranged from $0.4\,\mathrm{MeV}$ to $20\,\mathrm{MeV}$.

(1) Default spectrum

As the initial solution, default spectrum contains prior information. The enrichment of prior information contributes to the probability that spectrum unfolding converges to the global optimal solution. Simulated spectrum [46] and uniform spectrum [47] are two commonly used default spectra. They respectively represent the maximum and minimum prior information about the distribution of neutron fluence spectrum.

For fast neutron spectroscopy performed in a laboratory, neutron fluence spectrum at the test position can be simulated with the whole laboratory modeled by the MC code. An unfolded spectrum close to the simulated one can be expected if simulated default spectrum is used. However, when deviation appears between unfolded and simulated spectra, it is difficult to judge whether the deviation comes from the distortion of simulated spectrum or the inaccuracy of spectrum unfolding. Besides, it is difficult to simulate the fluence spectrum for in-situ fast neutron spectroscopy. Uniform spectrum

has the same constant value for all its counts. It only exerts non-negative constraints on the solution. Therefore, uniform default spectrum has better applicability and improves the reliability of unfolded spectrum.

Both simulated and uniform spectra were used as default spectra in spectrum unfolding for neutrons with broad energy distributions. Their influence on recoil and CG spectrum unfolding was analyzed. Only uniform default spectrum was used in spectrum unfolding for mono-energetic neutrons since it was difficult to build the precise MC model of the accelerator laboratory.

(2) Chi-square

The chi-square limit should be set to an appropriate value. If this limit is too big, iterations will be insufficient and spectrum unfolding cannot reach the optimal resolution. It means that unfolded spectrum is "underfitted" and deviation will happen. If this limit is too small, iterations will be excessive and spectrum unfolding tends to lose physical signature. It means that unfolded spectrum is "overfitted" and oscillations will appear [48]. In this paper, chi-square limits were determined according to the initial chi-squares of default spectra. For recoil and CG spectrum unfolding, chi-square limits were set to 1 and 0.001 , respectively.

B. Unfolded spectra

Recoil and CG unfolded spectra for mono-energetic neutrons are illustrated in the upper row of Fig. 5. As the fluence of the incident neutron beam is absent, each of these spectra was normalized by its total count in order to examine its distribution. For $14.84\,\mathrm{MeV}$ neutrons, there is no CG unfolded spectrum due to the absence of measured CG spectrum. The lower row of Fig. 5 shows recoil and CG unfolded spectra for neutrons with broad energy distributions respectively generated by ^{241}Am$-$Be and ^{252}Cf. Simulated spectra at the test points were also shown for comparison. Details about spectrum simulation performed with the SuperMC software [49] can be found in our previous work [50]. The left two figures in the lower row were obtained with simulated guess spectra and the right two figures were obtained with flat guess spectra.

(1) Mono-energetic neutrons

A distinct peak emerges at E_n in each of the recoil and CG unfolded spectra, which reflects that the two kinds of spectrum unfolding are both practicable. Narrower peaks in the CG unfolded spectra indicate that CG spectrum unfolding possesses better energy resolution than recoil spectrum unfolding. As neutron energy increases, the information entropies of the three CG unfolded spectra are 2.13, 2.47 and 2.97, respectively. Non-zero counts discretely appear at the left side of the peaks in CG unfolded spectra for $2.5\,\mathrm{MeV}$ and $5\,\mathrm{MeV}$ neutrons. These counts are induced by multiple factors, such as the deviations between simulated and real response spectra, misclassification of neutrons and γ-rays, as well as background and electronic noises.

As measured recoil spectra are short of characteristic peaks, it is difficult for recoil spectrum unfolding to determine the energy and fluence of incident neutrons according to the measured recoil spectrum. Therefore, recoil unfolded spectrum tends to be dispersed. This trend is more obvious as neutron energy increases. Consequently, with the growth of neutron energy, information entropies of the four recoil unfolded spectra are respectively 2.62, 3.11, 4.73 and 4.82, while the peak at E_n gradually falls. Each of the first three information entropies is higher than that of CG unfolded spectrum, indicating that recoil unfolded spectra are more dispersed. Recoil spectrum unfolding is also sensitive to errors of the measured spectrum and response matrix. It leads to the abnormal high counts at the low energy region in the four recoil unfolded spectra.

(2) Neutrons with broad energy distributions

Table 1 shows the iterations of recoil and CG spectrum unfolding for the ^{241}Am$-$Be and ^{252}Cf sources using simulated and flat default spectra, respectively. Beneficial from the prior information, simulated default spectra result in much fewer iterations than flat default spectra. CG spectrum unfolding requires fewer iterations than recoil spectrum unfolding. It verifies that CGEs are helpful to reduce the complexity of the spectrum unfolding process.

Recoil and CG unfolder spectra in the lower row of Fig. 5 are basically consistent with simulated spectra. It proves that for neutron with broad energy distributions, the two kinds of spectrum unfolding are both feasible with simulated or flat default spectra. According to Eq. (7), the lower limit of 0.05 MeVee corresponds to a threshold of about $0.4\,\mathrm{MeV}$. Therefore, unfolded spectrum using flat guess spectrum approximately has zero fluence rates below this threshold. Unfolded spectrum obtained with the simulated default spectrum could have non-zero fluence rates below this threshold because the default spectrum is close to global optimal solution and its energy distribution at this region possibly undergoes just a slight change after spectrum unfolding iterations.

Due to the sufficient prior information of simulated default spectra, recoil and CG unfolded spectra for the ^{241}Am$-$Be source revive the high fluence rates at the vicinities of $3\,\mathrm{MeV}$, $5\,\mathrm{MeV}$, $7.8\,\mathrm{MeV}$ and $10\,\mathrm{MeV}$, which are produced by the energy structure of ^{13}C. Consequently, recoil and CG unfolded spectra agree well with the simulated spectrum and their R^2 are respectively 0.951 and 0.988 above $0.4\,\mathrm{MeV}$. For the ^{252}Cf source, R^2 of recoil and CG unfolded spectra are respectively 0.969 and 0.879 above above $0.4\,\mathrm{MeV}$. CG unfolded spectrum receives smaller R^2 due to the lower fluence rate at low energy region. When the energy limit is lifted to $1\,\mathrm{MeV}$, R^2 of the two unfolded spectra become 0.953 and 0.986, respectively. Multiple parameters can be calculated with the unfolded spectrum. For instance, the total fluence rates of recoil and CG unfolded spectra for the ^{241}Am$-$Be source are respectively $149.01\,\mathrm{cm^{-2}s^{-1}}$ and $191.76\,\mathrm{cm^{-2}s^{-1}}$. Deviations from the total fluence rate of the simulated spectrum are -17.48% and 6.20%, respectively.

Discrepancy between unfolded and simulated spectra possibly comes from multiple factors, such as insufficient precision of MC model, fluctuation of measured spectrum and distortion of response matrix. Fluence rates of the recoil unfolded spectrum are smaller than those of the simulated spec-

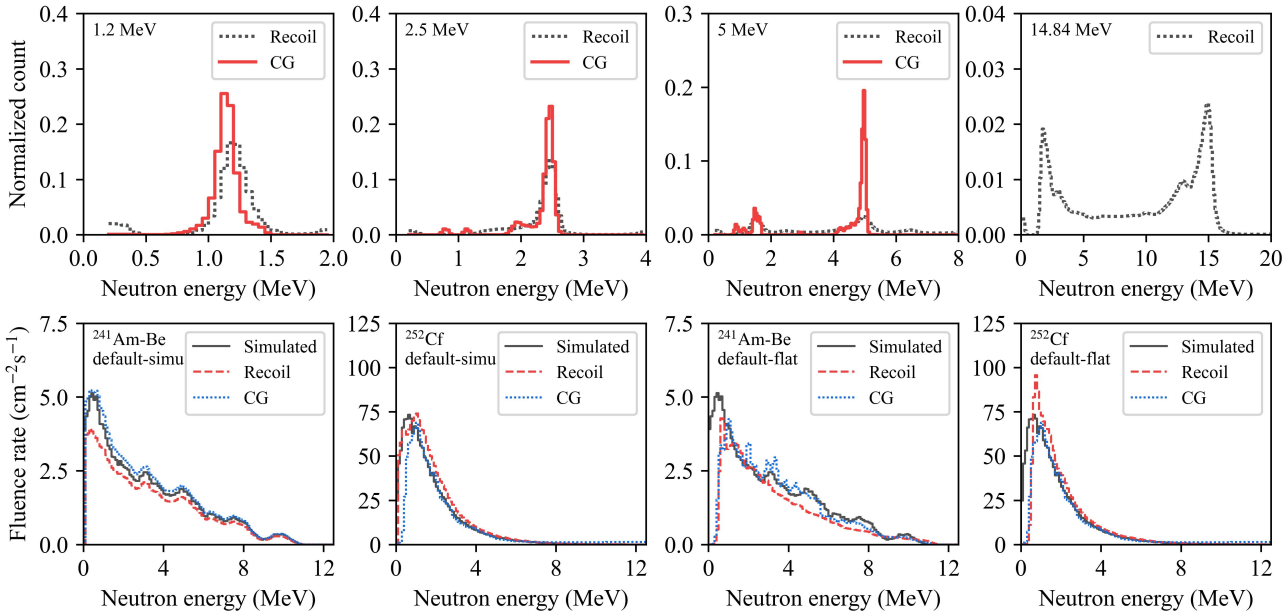

Fig. 5. Recoil and CG unfolded spectra for mono-energetic neutrons (upper row) and neutrons with broad energy distributions (lower row)

TABLE 1. Iterations of spectrum unfolding for the two neutron sources

Spectrum unfolding	Simulated default spectra		Flat default spectra	
	^{241}Am–Be	^{252}Cf	^{241}Am–Be	^{252}Cf
Recoil	1263	311	10 000	10 000
CG	5	13	380	78

trum for the ^{241}Am–Be source. This relationship is basically reversed for the ^{252}Cf source. However, CG unfolded spectrum does not encounter this reversal for the two sources. It indicates that compared with CG spectrum unfolding, recoil spectrum unfolding is accompanied by larger uncertainty due to higher sensitivity to errors in measured spectrum and response matrix.

Recoil and CG unfolded spectra undergo remarkable changes after flat default spectra are used. Their R^2 for the ^{241}Am–Be source above 0.4 MeV respectively decrease to 0.775 and 0.831, since unfolded spectra have nearly zero fluence rates below this threshold. If the energy limit is lifted to 1 MeV, R^2 become to 0.939 and 0.975, respectively. Recoil unfolded spectrum is smooth at the vicinities of 3 MeV, 5 MeV, 7.8 MeV and 10 MeV. Meanwhile, CG unfolded spectrum successfully restores the high fluence rates at these regions. It reflects that CG spectrum unfolding has better energy resolution and less reliance on prior information. For the ^{252}Cf source, R^2 of recoil and CG unfolded spectra are respectively 0.963 and 0.986 above 1 MeV. After the exchange of default spectrum, CG unfolded spectrum basically remains unchanged. However, fluence rates of recoil unfolded spectrum between 0.4 MeV and 1 MeV dramatically increase since fluence rates below 0.4 MeV fall to zero.

VI. SUMMARY

Fast neutron spectroscopy is required to operate nuclear power plants and other nuclear facilities. Organic scintillators have been widely used to realize recoil fast neutron spectroscopy. However, the corresponding spectrum unfolding is difficult as organic scintillators have flat response to mono-energetic neutrons. To address this issue, composite scintillators consisting of organic and inorganic scintillators have been proposed. These detectors can generate CGEs, which form a characteristic peak in the response. Taking advantage of this feature, CG fast neutron spectroscopy has been proposed in order to alleviate the difficulty of spectrum unfolding. Present composite scintillators are based on plastic scintillators and have poor triple discrimination performance. Besides, the influence of CCEs remains to be eliminated. Limited by these two factors, CG fast neutron spectroscopy has not been fully realized.

In this paper, CG fast neutron spectroscopy is fully realized for the first time based on a composite scintillator proposed in our previous work. This detector has excellent triple discrimination performance. Measured CG spectrum was obtained after the subtraction of CC spectrum from coincidence spectrum. The total count of measured CG spectrum is smaller than that of measured recoil spectrum by about three orders of magnitude. Its recoil and CG response matrices were established through MC simulations. The good agreement between

measured and simulated spectra to mono-energetic neutrons verified these simulations. In CG response matrix, characteristic peaks generated by neutrons with different energies converge into a ridge line. Using the MAXED code, recoil and CG spectrum unfolding was performed for mono-energetic neutrons and neutrons with broad energy distributions. Results show that recoil and CG spectrum unfolding are both practicable for the composite scintillator. Parameters such as total fluence rate can be calculated based on the unfolded spectrum. CG unfolded spectra for mono-energetic neutrons possess narrower peaks and lower information entropies. Compared with recoil fast neutron spectroscopy, CG fast neutron spectroscopy can reduce the number of iterations by at least an order of magnitude. CG unfolded spectra are more consistent with the simulated ones than recoil unfolded spectra. When flat default spectrum is used for the ^{241}Am–Be source, R^2 of recoil and CG unfolded spectra are respectively 0.939 and 0.975. Besides, CG unfolded spectrum successfully restore the high fluence rates at the vicinities of 3 MeV, 5 MeV, 7.8 MeV and 10 MeV, while recoil unfolded spectrum is smooth at these regions. Therefore, CG fast neutron spectroscopy can significantly alleviate the difficulty of spectrum unfolding and has better energy resolution and precision, compared with recoil fast neutron spectroscopy. Next, the CGE efficiency will be improved through the optimization of composite scintillator and pulse collection.

[1] ICRP Publication 116, *Conversion coefficients for radiological protection quantities for external radiation exposures*. (Elsevier, Amsterdam, 2010)

[2] H.H. Xiong, T.S. Li, S.Z. Chen et al., Investigation of an online reactor neutron spectrum measurement method with ionization chambers. Nucl. Technol. **202**, 94–100 (2018). doi:10.1080/00295450.2017.1419780

[3] Y.M. Zhang, L.J. Ge, Z.M. Hu et al., The first experimental results of time-of-flight neutron spectrometer at EAST. J. Fusion Energ. **40**, 14 (2021). doi:10.1007/s10894-021-00304-6

[4] Y.H. Chen, G.Y. Luan, J. Bao et al., Neutron energy spectrum measurement of the Back-n white neutron source at CSNS. Eur. Phys. J. A **55**, 115 (2019). doi: 10.1140/epja/i2019-12808-1

[5] M.L. Litvak, I. G. Mitrofanov, D. V. Golovin et al., Long-period variations of the neutron component of the radiation background in the area of the international space station according to the data of the BTN-neutron space experiment. Cosmic Res. **60**, 174–184 (2022). doi:10.1134/S0010952522030054

[6] Y.N. Liu, Z.Q. Wang, C.J. Li et al., Establishment of simulated neutron reference radiation field for workplaces of pressurized water reactor. At. Energy Sci. Technol. **54**, 2476–2480 (2020). doi:10.7538/yzk.2020.youxian.0465

[7] G.F. Knoll. *Radiation detection and measurement*, 4th edn. (John Wiley & Sons, New York, 2010)

[8] C.W. Li, H.Z. Zhou, H.X. Liu et al., Neutron spectrometry of D_2O-moderated ^{252}Cf with Bonner sphere spectrometer. Appl. Radiat. Isot. **197**, 110824 (2023). doi: 10.1016/j.apradiso.2023.110824

[9] Z.M. Hu, L.J. Ge, J.Q. Sun et al., Measurements of cosmic ray induced background neutrons near the ground using a Bonner sphere spectrometer. Nucl. Instrum. Methods Phys. Res., Sect. A **940**, 78–82 (2019). doi: 10.1016/j.nima.2019.06.004

[10] B. Liu, H.R. Yang, H.W. Lv et al., Neutron spectrum unfolding of the multiple activation foils based on sparse representation. Ann. Nucl. Energy **135**, 106947 (2020). doi: 10.1016/j.anucene.2019.106947

[11] S. Badiei, M.R. Kardan, G. Raisali et al., Unfolding of fast neutron spectra by superheated drop detectors using Adaptive Network-Based Fuzzy Inference System (ANFIS). Nucl. Instrum. Methods Phys. Res., Sect. A **944**, 162517 (2019). doi: 10.1016/j.nima.2019.162517

[12] F. Molina, P. Aguilera, J. Romero-Barrientos et al., Energy distribution of the neutron flux measurements at the Chilean Reactor RECH-1 using multi-foil neutron activation and the Expectation Maximization unfolding algorithm. Appl. Radiat. Isot. **129**, 28–34 (2017). doi: 10.1016/j.apradiso.2017.08.001

[13] Y.L Xiao, Z.X. Gu, Q.X. Zhang et al., New semi-analytical algorithm for solving PKEs based on Euler-Maclaurin approximation. Ann. Nucl. Energy **141**, 107308 (2020). doi: 10.1016/j.anucene.2020.107308

[14] R. Batchelor, R. Aves, T. H. R. Skyrme, Helium-3 filled proportional counter for neutron spectroscopy. Rev. Sci. Instrum. **26**, 1037–1047 (1955). doi: 10.1063/1.1715182

[15] D.H. Hou, S.Y. Zhang, Y.G. Yang, et al., Neutron measurement and inversion based on CLYC scintillator. J. Beijing Univ. Aeronaut. Astronaut. **47**, 106–114 (2021). doi: 10.13700/j.bh.1001-5965.2019.0643

[16] J. Liu, H.Y. Jiang, Z.Q. Cui, et al., Simultaneous measurement of energy spectrum and fluence of neutrons using a diamond detector. Sci. Rep. **12**, 12022 (2022). doi: 10.1038/s41598-022-16235-x

[17] G. Pichenot, S. Guldbakke, B. Asselineau et al., Characterisation of spherical recoil proton proportional counters used for neutron spectrometry. Nucl. Instrum. Methods Phys. Res., Sect. A **476**, 165–169 (2002). doi: 10.1016/S0168-9002(01)01424-3

[18] Y.H. Chen, Y.J. Qiu, Q. Li et al., Measurement of the neutron flux of CSNS Back-n ES#1 under small collimators from 0.5 eV to 300 MeV. Eur. Phys. J. A **60**, 63 (2024). doi: 10.1140/epja/s10050-024-01272-z

[19] X. Yuan, X. Zhang, X. Xie et al., Neutron energy spectrum measurements with a compact liquid scintillation detector on EAST. J. Instrum. **8**, P07016 (2013). doi: 10.1088/1748-0221/8/07/P07016

[20] R. He, X.Y. Niu, H.W. Liang et al., Advances in nuclear detection and readout techniques. Nucl. Sci. Tech. **34**, 205 (2023). doi: 10.1007/s41365-023-01359-0

[21] T. He, P. Zheng, J. Xiao, Measurement of the prompt neutron spectrum from thermal-neutron-induced fission in U-235 using the recoil proton method. Nucl. Sci. Tech. **30**, 112 (2019). DOI: 10.1007/s41365-019-0633-z

[22] S.Y. Zhang, X. Yang, Y.X. Wang et al., Measurement of neutron source characterization of the compact D–D neutron generator with unfolding algorithm. Eur. Phys. J. A **59**, 101 (2024). doi: 10.1140/epja/s10050-023-01007-6

[23] C.C. Lawrence, M. Febbraro, M. Flaska et al., Warhead verification as inverse problem: Applications of neutron spectrum unfolding from organic-scintillator measurements. J. Appl. Phys. **120**, 064501 (2016). doi: 10.1063/1.4960131

[24] H.Y. Bai, Z.M. Wang, L.Y. Zhang et al., Calibration of an

EJ309 liquid scintillator using an AmBe neutron source. Nucl. Instrum. Methods Phys. Res., Sect. A **863**, 47–54 (2017). doi: 10.1016/j.nima.2017.04.028

[25] C. Liao, H.R. Yang, n/γ Pulse shape discrimination comparison of EJ301 and EJ339A liquid scintillation detectors. Ann. Nucl. Energy **69**, 57–61 (2014). doi: 10.1016/j.anucene.2014.01.039

[26] Y.K. Sun, H. Zhang, X.K. Zhao et al., Identifying thermal neutrons, fast neutrons, and gamma rays by using a scintillator-based time-of-flight method. Nucl. Instrum. Methods Phys. Res., Sect. A **940**, 129–134 (2019). doi: 10.1016/j.nima.2019.06.027

[27] J.B. Czirr, G.L. Jensen, A neutron coincidence spectrometer. Nucl. Instrum. Methods Phys. Res., Sect. A **284**, 365–369 (1989). doi: 10.1016/0168-9002(89)90303-3

[28] S. Hunt, C. Iliadis, R. Longland, Characterization of a ^{10}B-doped liquid scintillator as a capture-gated neutron spectrometer. Nucl. Instrum. Methods Phys. Res., Sect. A **811**, 108–114 (2016). doi: 10.1016/j.nima.2015.12.001

[29] T.J. Langford, E.J. Beise, H. Breuer et al., Development and characterization of a high sensitivity segmented Fast Neutron Spectrometer (FaNS-2). J. Instrum. **11**, P01006 (2016). doi: 10.1088/1748-0221/11/01/P01006

[30] H.X. Huang, B. Gao, Y.T. Li et al., Low event rate neutron detector array using the coincidence between plastic scintillator and Helium-3 proportional counters. Nucl. Instrum. Methods Phys. Res., Sect. A **1003**, 165323 (2021). doi: 10.1016/j.nima.2021.165323

[31] W. Li, M.R. Tao, Y.Y. Li et al., NaI:Tl,^{6}Li-PVT composite scintillator toward neutron and gamma discrimination. Radiat. Meas. **159**, 106882 (2022). doi: 10.1016/j.radmeas.2022.106882

[32] M. Mayer, J. Nattress, V. Kukharev et al., Development and characterization of a neutron detector based on a lithium glass–polymer composite. Nucl. Instrum. Methods Phys. Res., Sect. A **785**, 117–122 (2015). doi: 10.1016/j.nima.2015.03.014

[33] K. Wilhelm, J. Nattress, I. Jovanovic, Development and operation of a ^{6}LiF :ZnS(Ag)-scintillating plastic capture-gated detector. Nucl. Instrum. Methods Phys. Res., Sect. A **842**, 54–61 (2017). doi: 10.1016/j.nima.2016.10.042

[34] J. Nattress, M. Mayer, A. Foster et al., Capture-gated spectroscopic measurements of monoenergetic neutrons with a composite scintillation detector. IEEE Trans. Nucl. Sci. **63**, 1227–1235 (2016). doi: 10.1109/TNS.2016.2537761

[35] H.Z. Zhou, W.Y. Xiao, T. Sun et al., Simultaneous detection of fast and thermal neutrons with a stilbene-^{6}Li glass composite scintillator. Nucl. Instrum. Methods Phys. Res., Sect. A **1054**, 168396 (2023). doi: 10.1016/j.nima.2023.168396

[36] M. Sharma, J. Nattress, K. Wilhelm et al., Triple pulse shape discrimination and capture-gated spectroscopy in a composite heterogeneous scintillator. Nucl. Instrum. Methods Phys. Res., Sect. A **857**, 75–81 (2017). doi: 10.1016/j.nima.2017.03.019

[37] A. Foster, A. Meddeb, M. Wonders et al., On the fabrication and characterization of heterogeneous composite neutron detectors with triple-pulse-shape-discrimination capability.Nucl. Instrum. Methods Phys. Res., Sect. A **954**, 161681 (2020). doi: 10.1016/j.nima.2018.11.140

[38] F. Pino, J.C. Delgado, S.M. Carturan et al., Novel flexible and conformable composite neutron scintillator based on fully enriched lithium tetraborate. Sci. Rep. **13**, 4799 (2023). doi: 10.1038/s41598-023-31675-9

[39] H.Z. Zhou, T. Sun, H.X. Liu et al., Chance coincidence analysis for capture-gated neutron spectrometry with a composite scintillator. Instrum. Methods Phys. Res., Sect. A **1056**, 168636 (2023). doi: 10.1016/j.nima.2023.168636

[40] L. Swiderski, M. Moszyński, W. Czarnacki et al., Measurement of Compton edge position in low-Z scintillators. Radiat. Meas. **45**, 605–607 (2010). doi: 10.1016/j.radmeas.2009.10.015

[41] H.Z. Zhou, W.Y. Xiao, H.X. Liu et al., A linear separation method for neutrongamma discrimination with organic scintillators. Instrum. Methods Phys. Res., Sect. A **1048**, 167879 (2023). doi: 10.1016/j.nima.2022.167879

[42] S. Agostinelli, J. Allison, K. Amako et al., Geant4—a simulation toolkit. Instrum. Methods Phys. Res., Sect. A **506**, 250–303 (2003). doi: 10.1016/S0168-9002(03)01368-8

[43] R.A. Weldon Jr., J.M. Mueller, C. Awe et al., Characterization of stilbene's scintillation anisotropy for recoil protons between 0.56 and 10 MeV. Instrum. Methods Phys. Res., Sect. A **977**, 164178 (2020). doi: 10.1016/j.nima.2020.164178

[44] A. Enqvist, C.C. Lawrence, B.M. Wieger et al., Neutron light output response and resolution functions in EJ-309 liquid scintillation detectors. Instrum. Methods Phys. Res., Sect. A **715**, 79–86 (2013). doi: 10.1016/j.nima.2013.03.032

[45] Y.X. Zhuang, T.J. Liu, J.S. Zhang et al., CENDL-3 – Chinese evaluated nuclear data library, version 3. J. Nucl. Sci. Technol. **39**, 37–39 (2002). doi: 10.1080/00223131.2002.10875033

[46] M. Reginatto, B. Wiegel, A. Zimbal et al., UMG 3.3, Analysis of data measured with spectrometers using unfolding techniques. NEA (2004).

[47] M. Reginatto, A. Zimbal, Bayesian and maximum entropy methods for fusion diagnostic measurements with compact neutron spectrometers. Rev. Sci. Instrum. **79**, 023505 (2008). doi: 10.1063/1.2841695

[48] L. Giacomelli, M. Reginatto et al., Optimization of MAXED input parameters with applications to the unfolding of neutron diagnostics data from the Joint European Torus. Rev. Sci. Instrum. **90** 093505 (2019). doi: 10.1063/1.5097784

[49] Y.C. Wu, S.P. Yu, M.Y. Cheng et al., Design and implementation of multi-physics coupling analysis modeling program SuperMC/MCAM5.2. At. Energy Sci. Technol. **49**, 1–6 (2015). doi:10.7538/yzk.2015.49.S0.0001

[50] H.X. Liu, T. Sun, C.W. Li et al., Design and testing of an irradiation room with low room-scattering for neutron calibration. Appl. Radiat. Isot. **211**, 111402 (2024). doi: 10.1016/j.apradiso.2024.111402